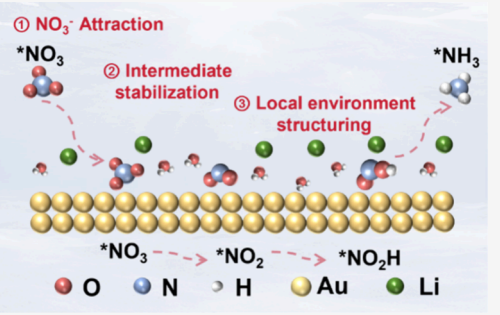
JACS
JOURNAL OF THE AMERICAN CHEMICAL SOCIETY
pubs.acs.org/JACS
Article

Deciphering Cation-Stabilized *NO_2 at the Molecular Level in Electrocatalytic Nitrate Reduction

Ru-Yu Zhou,[§] Shisheng Zheng,[§] Rui Ma, Yao-Hui Wang,* Mengting Zhao, Chongyuan Zhai, Jin-Chao Dong, Feng Pan,* and Jian-Feng Li*

Cite This: J. Am. Chem. Soc. 2026, 148, 425−433
Read Online
ACCESS | Metrics & More | Article Recommendations | Supporting Information

ABSTRACT: Electrochemical nitrate reduction (NO_3RR) offers a sustainable pathway for ammonia (NH_3) production, yet its advancement is limited by a lack of molecular-level understanding of interfacial reaction dynamics. Here, we unravel a synergistic interfacial mechanism for rational catalyst design based on cooperative interfacial modulation. By integrating in situ Raman spectroscopy with multiscale simulations, we uncover a cation-mediated stabilization mechanism of the key *NO_2 intermediate on atomically defined Au single-crystal surfaces. We demonstrate that electrolyte cations play a critical role in modulating the local electric field and stabilizing *NO_2 via interfacial coordination, thereby controlling its interfacial reactivity and subsequent transformation. Armed with this insight, we employ Sn heteroatom modification to achieve dual-function optimization. The electronic interaction between Sn and Au weakens *NO_2 adsorption, lowering the hydrogenation barrier, while the altered interfacial water structure facilitates proton transfer through a reinforced hydrogen-bond network. This synergistic modulation leads to enhanced NH_3 selectivity and suppressed hydrogen evolution. Our findings highlight a paradigm shift from an active-site-centric catalyst design to an integrated approach that considers the entire electrochemical interface, where electronic, ionic, and solvent effects are concurrently tuned. This work provides both molecular-level mechanistic insights and a generalizable strategy for designing advanced electrocatalysts for NO_3RR and broader proton-coupled electron transfer reactions.



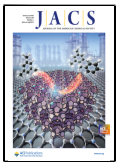
INTRODUCTION

Excessive nitrate (NO_3^-) accumulation in water bodies and the fossil-driven production of ammonia (NH_3) pose serious environmental and energy challenges.[1,2] Beyond its role as a vital fertilizer, NH_3 is gaining attention as a carbon-free energy carrier for direct ammonia fuel cells (DAFCs), offering high energy density and compatibility with existing infrastructure.[3] Addressing both NO_3^- pollution and clean NH_3 synthesis simultaneously has thus become a strategic objective in sustainable nitrogen management, challenging the sustainability of the conventional Haber-Bosch synthesis.[4,5] Electrochemical nitrate reduction (NO_3RR) offers a promising route, enabling decentralized NH_3 production under ambient conditions while mitigating water contamination.[6−8]

Despite recent progress, achieving high NH_3 selectivity and activity at practical current densities remains elusive. The NO_3RR pathway involves intricate multistep proton−electron transfers and the stabilization of short-lived nitrogenous intermediates, such as *NO_x species. Two fundamental limitations prevail in poor stabilization of key intermediates under negative potentials and sluggish hydrogenation kinetics due to limited proton availability at the interface.[9] Therefore, unraveling the precise, multifaceted role of cations in governing the NO_3RR pathway, and leveraging that knowledge for rational catalyst design, is a central goal.[10]

The overall NO_3RR process is a delicate balance between two competing yet sequential reaction types: deoxygenation of N−O bonds and hydrogenation of the resulting nitrogen-containing intermediates.[11] The deoxygenation steps are intricately linked to the adsorption energy and electronic properties of *NO_x species at the active sites. Conversely, the hydrogenation steps are critically dependent on a steady supply of active hydrogen (*H), typically derived from water dissociation in aqueous media.[12] This duality creates a fundamental challenge that catalysts highly efficient for water splitting often suffer from excessive *H coverage, which blocks the adsorption sites for *NO_x and favors the parasitic hydrogen evolution reaction (HER).[13,14] Consequently, achieving high NH_3 selectivity, especially at industrially relevant ampere-level current densities, demands a sophisticated catalyst design that

Received: August 13, 2025
Revised: December 15, 2025
Accepted: December 18, 2025
Published: December 26, 2025



Downloaded from pubs.acs.org/jacsat/article-pdf/148/1/425/6372241/ja5c13376.pdf by UNIV TOWN OF SHENZHEN user on 08 September 2026

© 2025 American Chemical Society

https://doi.org/10.1021/jacs.5c13376
J. Am. Chem. Soc. 2026, 148, 425−433

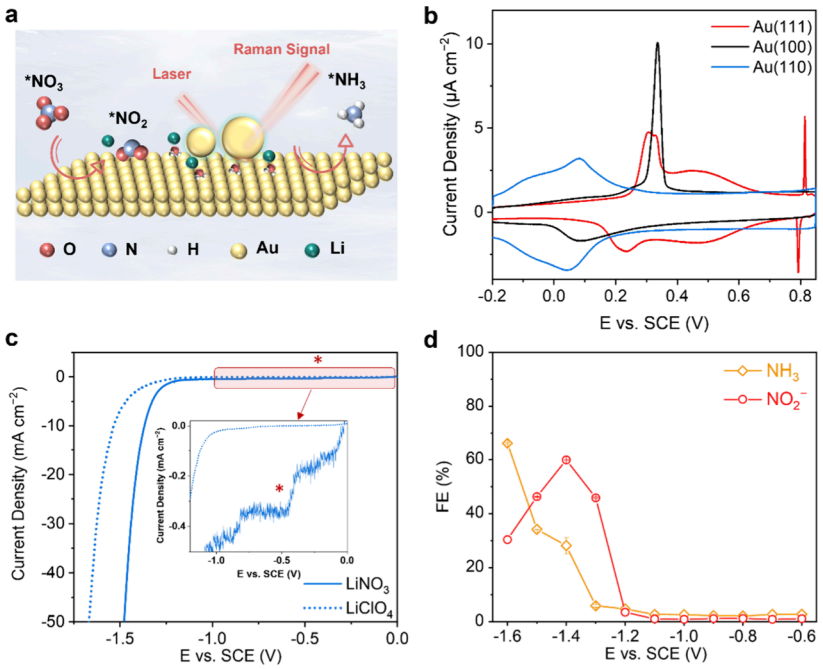


Figure 1. NO_3RR on $LiNO_3$–Au(111) interface. (a) Schematic illustration of in situ SHINERS experiment. (b) CV of Au(hkl) in 0.05 M H_2SO_4 with the scan rate of 10 mV s^{-1}. (c) LSV of Au(111) in 5.05 M $LiClO_4$ and $LiNO_3$ electrolytes. (d) Potential-dependent Faradaic efficiency (FE) of NH_3 and NO_2^- on Au(111) in 5.05 M $LiNO_3$.

can synergistically orchestrate the kinetics of both deoxygenation and hydrogenation.

Recent theoretical studies suggest that electrolyte cations play a vital role in activating NO_3^- by modulating the local electrostatic environment.[15] The strong electrostatic stabilization from cations is indispensable for overcoming the repulsion between the anionic NO_3^- and a negatively polarized electrode surface. Building on this, materials design strategies have been developed. For instance, Sn-modified Pt/Pd surfaces have been shown to stabilize $*NO_2$ through electronic modulation, while strain engineering in Cu/CuAu core–shell nanostructures is reported to enhance the initial $*NO_3$ activation.[16,17] Other key intermediates like nitric oxide (*NO) and nitroxyl (*NHO) are also proposed to play crucial roles in orchestrating the complex multistep hydrogenation cascade, yet their precise roles and interactions remain debated.[18] While these works have advanced NO_3RR efficiency by targeting specific N-containing intermediates,[19,20] a profound knowledge gap persists. Direct experimental evidence capturing these interfacial effects at the molecular level, especially on well-defined catalytic surfaces, remains scarce. Conventional studies using polycrystalline electrodes or ex situ characterizations often obscure intrinsic reactivity with surface heterogeneity and mass transport limitations.[21]

Herein, we integrate in situ Shell-Isolated Nanoparticle-Enhanced Raman Spectroscopy (SHINERS) with multiscale simulations to unravel the NO_3RR mechanism on atomically flat Au single-crystal electrodes.[22−24] We identify $*NO_2$ as the central reaction intermediate and reveal a previously underappreciated cation-stabilization mechanism that governs its accumulation. Guided by this insight, we introduce Sn heteroatom modification to simultaneously modulate electronic interactions and restructure interfacial hydrogen bonding. This dual-function strategy enables efficient $*NO_2$ hydrogenation and suppresses competing hydrogen evolution, offering a generalizable framework for rational catalyst and interface design.

RESULTS AND DISCUSSION

Elucidating the Interfacial Puzzle of NO_3RR on Au Single-Crystal. We began by evaluating the electrochemical activity of NO_3RR on atomically flat Au single-crystal surfaces. The Au(hkl) electrodes were prepared by the Clavilier method,[25] a standard procedure for obtaining atomically flat and well-ordered single-crystal surfaces. The atomic-level flatness and long-range order of our primary model surface, Au(111), were fundamentally demonstrated by Scanning Tunneling Microscopy (STM) in Figure S21a. The quality and long-range order of these surfaces were further corroborated by their characteristic cyclic voltammetry (CV) profiles in Ar-saturated 0.05 M H_2SO_4 (Figure 1b). The sharp, well-defined voltammetric features are uniquely sensitive to the atomic arrangement of the specific crystal facet and serve as a reliable indicator of a high-quality surface. The well-resolved surface features observed for Au(111), Au(110), and Au(100) indicate excellent crystallinity and surface order, validating these model electrodes as ideal platforms for probing intrinsic interfacial behavior.[26] Comparative linear sweep voltammetry (LSV) in 5.05 M $LiNO_3$ and $LiClO_4$ electrolytes (Figure 1c) shows that a distinct reduction peak emerges exclusively in NO_3^--containing electrolytes (inset in Figure 1c). This comparison serves as a critical control experiment, demonstrating that the observed current is due to the reduction of the NO_3^- anion, as the electrochemically inert ClO_4^- anion does not produce a similar signal under these conditions. The anion-specific nature of this process, along with the potential-dependent production of NH_3 and NO_2^- (Figure 1d), establishes a mechanistic basis for investigating key reaction intermediates.

To directly probe the interfacial intermediates on Au single-crystal surfaces in Ar-saturated $LiNO_3$ electrolytes, we

Downloaded from pubs.acs.org/jacsat/article-pdf/148/1/425/6337224/1/ja5c13376.pdf by UNIV TOWN OF SHENZHEN user on 08 September 2026

https://doi.org/10.1021/jacs.5c13376
J. Am. Chem. Soc. 2026, 148, 425−433

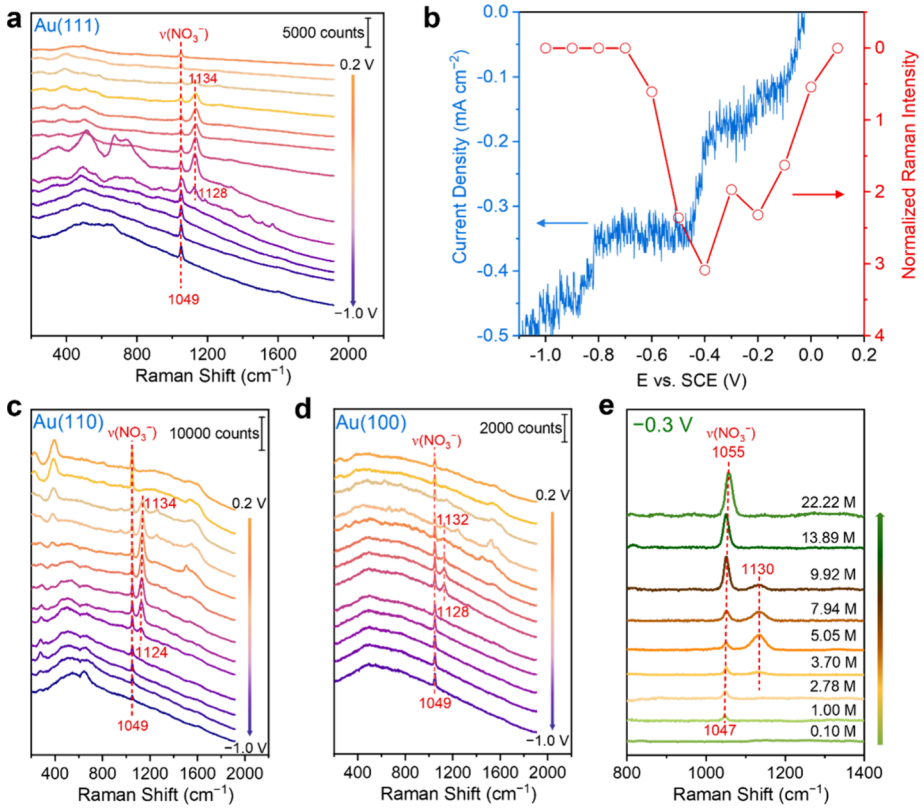


Figure 2. In situ Raman spectra of potential-dependent intermediate evolution. (a) Potential-dependent intermediate evolution on Au(111), in 5.05 M $LiNO_3$ tracked by SHINERS. (b) Normalized Raman intensities of peak 1128 ~ 1134 cm^{-1} on Au(111) in 5.05 M $LiNO_3$, plotted together with LSV curve. (c) In situ Raman spectra on Au(110). (d) In situ Raman spectra on Au(100). (e) The Raman spectra of intermediate at − 0.3 V on Au(111) in $LiNO_3$ with varying concentrations.

employed in situ electrochemical SHINERS. As illustrated in Figure 1a and experimental section in the Supporting Information, a monolayer of pinhole-free Au@SiO_2 nanoparticles was assembled on the Au(hkl) surfaces (Figure 1a and Figure S1). While at 0.2 V vs SCE, only the symmetric N−O stretching mode of NO_3^- at 1049 cm^{-1} was detected on Au(111) in 5.05 M $LiNO_3$ (Figure 2a).[27] Upon cathodic polarization to −0.1 V, a prominent Raman peak emerged at 1134 cm^{-1}. The peak gradually red-shifted with decreasing cathodic potential and was referred to as the 1130 cm^{-1} peak. The intensity followed a volcano-shaped trend with potential, peaking near −0.5 V and declining at more negative potentials. This potential-dependent behavior indicates a transient intermediate that accumulates and is subsequently consumed. The peak intensity of the intermediate was normalized to the intensity of the symmetric stretching mode of NO_3^- (~1049 cm^{-1}) to account for any variations in signal collection efficiency (Figure 2b). Notably, the evolution of this peak closely matched the NO_3^- reduction current and the NH_3 production rate, strongly supporting its assignment as a kinetically relevant intermediate. Similar behavior was observed on all three low-index Au facets (Figures 2c,d), underscoring its general significance.

We further examined the effect of electrolyte concentration on intermediate stability over a wide range (from 0.10 to 22.22 M). A nonmonotonic trend was observed (Figure 2e and Figures S8−S15). In both dilute (e.g., ≤1.00 M) and superconcentrated (e.g., ≥13.89 M) $LiNO_3$ solutions, the 1130 cm^{-1} peak was undetectable. However, the 1130 cm^{-1} peak emerged prominently at intermediate concentrations. The relative intensity of this peak, normalized to the N−O stretching band, reached a maximum at approximately 5.05 M, suggesting an optimal interfacial environment for stabilizing the transient species.

Identification of the *NO_2 Intermediate. To clarify the origin of the 1130 cm^{-1} band, we performed a series of control and isotopic labeling experiments. First, we examined potential contributions from other common electrolyte anions using $LiClO_4$, LiCl, Li_2SO_4, and $NaNO_2$ electrolytes under equivalent concentrations (Figure 3a,b and Figures S2−S7). In these systems, no signal was detected near 1130 cm^{-1}. For instance, the $LiClO_4$ spectrum displayed a characteristic ClO_4^- peak at 933 cm^{-1} (Figure 3a), but no sign of the targeted intermediate.[28] Similarly, LiCl (Figure S2) and Li_2SO_4 (Figure S3) electrolytes yielded no corresponding vibrational bands. In contrast, the same 1130 cm^{-1} feature was observed in $NaNO_2$ electrolyte, suggesting that NO_3^- and NO_2^- reduction may proceed through a shared intermediate (Figure 3b and Figure S7). Collectively, these results rule out Cl^-, ClO_4^-, or SO_4^{2-} as sources of the observed signal. The results strongly imply that the 1130 cm^{-1} peak is a common N-containing intermediate in both NO_3^- reduction pathways.

To assess the involvement of solvent molecules, we replaced H_2O with D_2O and observed no discernible frequency shift (Figure 3c and Figure S4), ruling out contributions from hydrogen atoms in water. Similarly, spectra obtained with $H_2{}^{18}O$ experiments showed negligible shifts, excluding water-derived oxygen from the vibrational origin (Figure S5). In contrast, when using ^{15}N-labeled $Na^{15}NO_3$ isotope (Figure 3c and Figure S6), the 1130 cm^{-1} peak underwent a pronounced

https://doi.org/10.1021/jacs.5c13376
J. Am. Chem. Soc. 2026, 148, 425−433

Downloaded from pubs.acs.org/jacsat/article-pdf/148/1/425/6337224/1/ja5c13376.pdf by UNIV TOWN OF SHENZHEN user on 08 September 2026

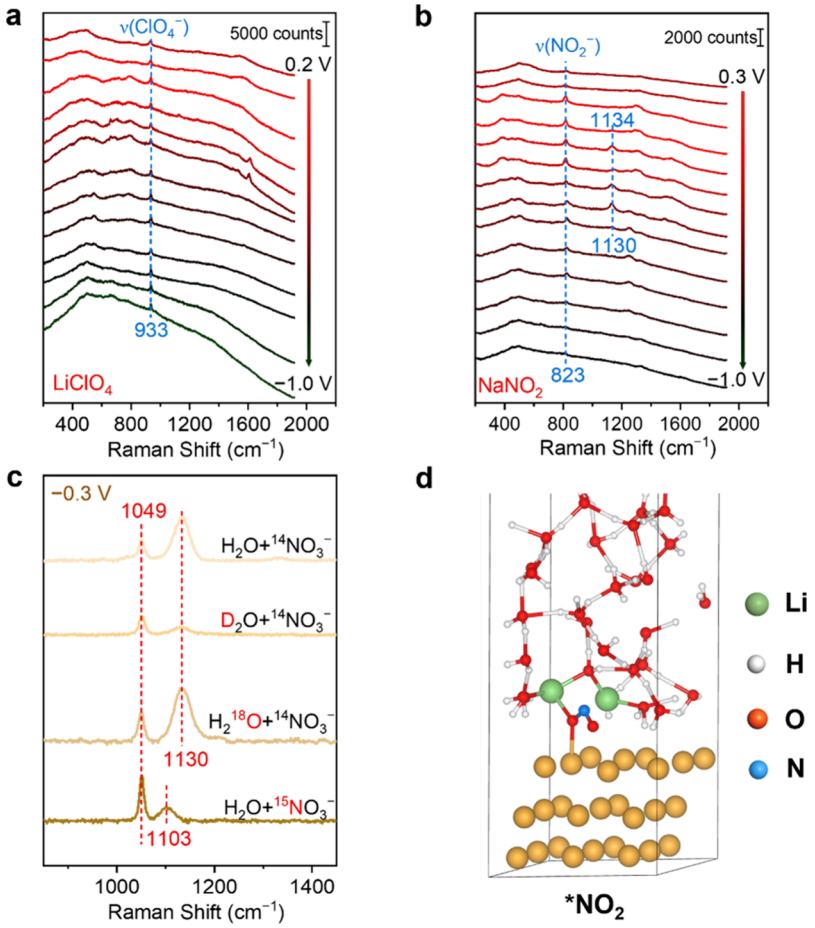


Figure 3. Identification of 1128 ~ 1134 cm^{-1} peak. (a) In situ Raman spectra on Au(111) in 5.05 M $LiClO_4$, (b) $NaNO_2$. (c) Raman spectra of H_2O, D_2O, $H_2{}^{18}O$, $^{15}NO_3^-$ isotope experiments at − 0.3 V. (d) Calculated adsorption configuration of $*NO_2$ on Au(111) surface.

redshift to 1103 cm^{-1}. This corresponds to an absolute frequency shift ($\Delta\nu$) of 27 cm^{-1} and an experimental frequency ratio ($\nu^{15}N/\nu^{14}N$) of 97.6%. This value is in agreement with the theoretically predicted ratio of 98.2% for an N−O stretching vibration based on the reduced mass in a simple harmonic oscillator model,[29] which further solidifies the assignment. The isotopic shift unambiguously assigns the 1130 cm^{-1} peak to a N-containing vibrational mode.

Having identified the intermediate as a nitrogen oxyanion, we turned to first-principles simulations to investigate its molecular structure. During the NO_3RR process, only the $*NO_2$ and *NO species satisfy the above-mentioned conditions. Density functional theory (DFT) calculations of the NO_3RR pathway revealed that $*NO_2$ is a key intermediate formed from the initial deoxygenation of $*NO_3$. This step represents the primary thermodynamic barrier, which is consistent with the accumulation of $*NO_2$ observed in Raman experiments at intermediate potentials, and therefore is most likely to occur under these conditions.

We further performed ab initio molecular dynamics (AIMD) simulations to calculate the vibrational density of states (VDOS) of $*NO_2$ and *NO at the interface. Our simulations reveal that $*NO_2$ adsorbs in a tilted geometry, with one oxygen atom covalently bonded to the Au surface and also coordinate with the hydrated Li^+ ion (Figure 3d). The time-evolution analysis confirms that this dual-interaction structure is stable throughout the simulation (see Figures S18 and S19 for details). This specific configuration, where the N−O bond is simultaneously influenced by the surface and the cation, weakens and polarizes its vibration. The resulting calculated VDOS peak at 1184 cm^{-1} is in close alignment with our experimentally observed peak at ~ 1130 cm^{-1}, providing strong theoretical validation for its assignment.[30] The AIMD simulations were run for a sufficient duration to ensure proper equilibration, as evidenced by the stable fluctuations of total energy and temperature over time (see Figures S27 and S28).

To elucidate the origin of the nonmonotonic proton-coupled electron transfer of the 1130 cm^{-1} peak, we examined the interfacial behavior of $*NO_2$ in varying electrolyte environments. The cation-coordination effect also elegantly explains the volcano-shaped dependence on electrolyte concentration (Figure 2e and Figure S15). To investigate whether the signal decline at superconcentrated conditions (e.g., > 10 M) could be attributed to a mass transfer limitation in the increasingly viscous electrolyte, we performed hydrodynamic voltammetry experiments. As detailed in the Supporting Information (Figure S20), the reduction current at 5.05 M shows negligible dependence on the electrode rotation speed. This result provides strong evidence that the reaction is not under mass transfer control. Therefore, the observed decline in the $*NO_2$ signal is not due to a limitation in NO_x supply. Instead, this reinforces our hypothesis that the interfacial environment itself becomes suboptimal.

We propose that at superconcentrated conditions, factors such as interfacial crowding and excessive Li^+ screening compress the electric double layer, disrupting the optimal

https://doi.org/10.1021/jacs.5c13376
J. Am. Chem. Soc. 2026, 148, 425−433

Downloaded from pubs.acs.org/jacsat/article-pdf/148/1/425/6337224/1/ja5c13376.pdf by UNIV TOWN OF SHENZHEN user on 08 September 2026

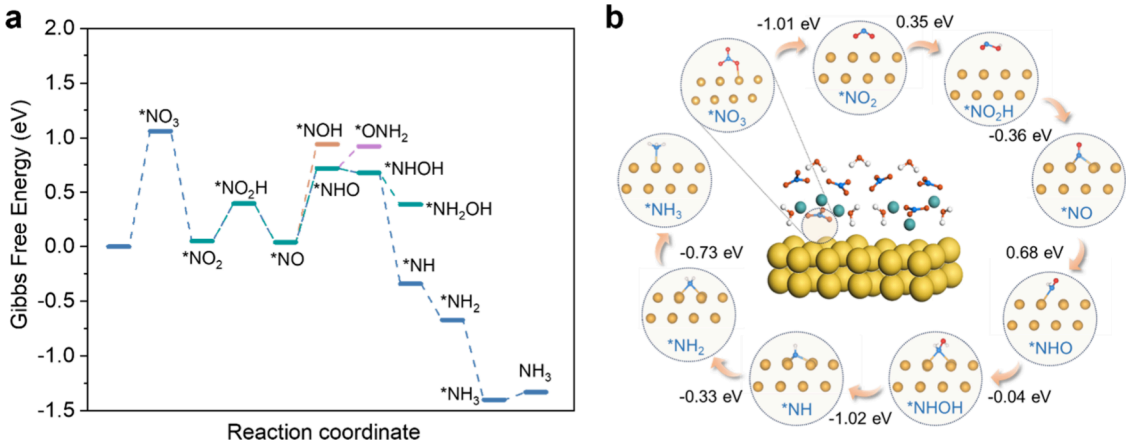


Figure 4. DFT-calculated reaction energetics of NO_3RR on Au(111). (a) Gibbs free energy profile of the stepwise NO_3RR pathway at pH = 7. The free energy of each elementary step was calculated based on the computational hydrogen electrode (CHE) model. The calculations were performed on a periodic Au(111) slab model. (b) Atomistic representations of key intermediates along the conversion sequence.

configuration required for effective $*NO_2$ modulation and leading to the downturn in the volcano plot. At intermediate concentration (around 5.05 M), Li^+ cations were found to accumulate at the interface and interacted with interfacial $*NO_2$ species through directional electrostatic coordination. This interaction enhanced $*NO_2$ stabilization, resulting in a strong vibrational signature consistent with experimental observations. At low concentrations, the scarcity of Li^+ in the interfacial region led to insufficient stabilization of $*NO_2$, thereby diminishing its spectroscopic signature (Figures S8–S10). Conversely, at superconcentrated concentrations, excessive Li^+ screening compressed the electric double layer and disrupted the optimal configuration required for effective $*NO_2$ coordination (Figure S14). These findings explain the observed volcano-shaped relationship between $LiNO_3$ concentration and the 1130 cm^{-1} Raman signal, and highlight the delicate balance between ionic strength and interfacial structuring in NO_3RR.

To gain deeper atomistic insights into the reaction energetics, we performed DFT calculations for the mechanistic pathways of NO_3RR on the Au(111) surface. While our spectroscopic results point to $*NO_2$ as the dominant reaction intermediate, it is crucial to acknowledge the complex nature of the electrified interface. Mechanistically, other surface species such as adsorbed hydrogen (*H) from the competing hydrogen evolution reaction, as well as adsorbed oxygen (*O) and hydroxyl (*OH) as byproducts of the initial N–O bond cleavage, are inevitably present. The Gibbs free energy diagram (Figure 4a), which accounts for the energetics of all transient species including the spectroscopically unobserved O and H participants, reveals the most thermodynamically favorable stepwise mechanism. Crucially, our calculations reveal that the subsequent first hydrogenation step, the conversion of $*NO_2$ to $*NO_2H$, requires surmounting a significant free energy change of ΔG = 0.35 eV. This theoretically identified barrier provides a direct and compelling rationale for our spectroscopic observations.[31,32] At potentials where NO_3RR begins, the facile formation of $*NO_2$ coupled with its thermodynamic bottleneck hindered consumption leads to the accumulation of this intermediate on the electrode surface. As the applied potential is swept to more negative values, this 0.35 eV bottleneck is progressively overcome, promoting the conversion of the accumulated $*NO_2$ and driving the reaction toward NH_3. Once this initial thermodynamic barrier is surmounted, the subsequent hydrogenation steps are largely downhill in free energy, proceeding rapidly via the most favorable pathway (*NO → *NHO → *NHOH → *NH). A detailed comparison of all calculated pathways is presented in Figure 4a, confirming this is the lowest-energy route. The final desorption of NH_3 into the solution is also a facile step (ΔG = 0.07 eV). This refined mechanistic insight, where the bottleneck is the consumption of $*NO_2$, not its formation, provides a seamless integration of our theoretical and experimental results.

To further validate this holistic model, we investigated the effect of cation identity by performing experiments in Na^+ and K^+ containing electrolytes (Figures S16 and S17). The results revealed a similar $*NO_2$ signal in 5.05 M $NaNO_3$, with no signal detected in 2.78 M KNO_3. This trend is perfectly rationalized by our two-stage model and the properties of the cations. Li^+, possessing the highest charge density among the series, is superior in all aspects. It is effective at attracting NO_3^- and provides strong anchoring for $*NO_2$ while most effectively structuring the local water environment to gate its consumption. These comparative findings firmly establish the cation as a pivotal governor of the entire interfacial reaction kinetics, orchestrating both the arrival of the reactant and the turnover of the key intermediate.

Sn Heteroatom Modification and Interfacial Engineering. The detailed mechanistic insights from the preceding section pinpoint a central design challenge for advanced NO_3RR electrocatalysts. Achieving high efficiency requires navigating the delicate kinetic balance of the $*NO_2$ intermediate: its accumulation must be fostered, while its kinetically demanding subsequent hydrogenation must be facilitated. This presents a dual-requirement challenge: an ideal catalyst surface must simultaneously (i) possess an optimized electronic structure to favorably interact with the $*NO_2$ adsorbate, and (ii) engineer the local solvent environment to ensure rapid proton delivery. To address this challenge, we hypothesized that a heteroatom modification strategy could provide an elegant solution. We rationally selected Sn as a strategic modifier, based on its known ability to both electronically perturb noble metal surfaces and, as an oxophilic element, to form a hydrophilic oxide layer capable of fundamentally restructuring the interfacial water network.[33–36]

Downloaded from pubs.acs.org/jacsat/article-pdf/148/1/425/6337224/1/ja5c13376.pdf by UNIV TOWN OF SHENZHEN user on 08 September 2026

https://doi.org/10.1021/jacs.5c13376
J. Am. Chem. Soc. 2026, 148, 425–433

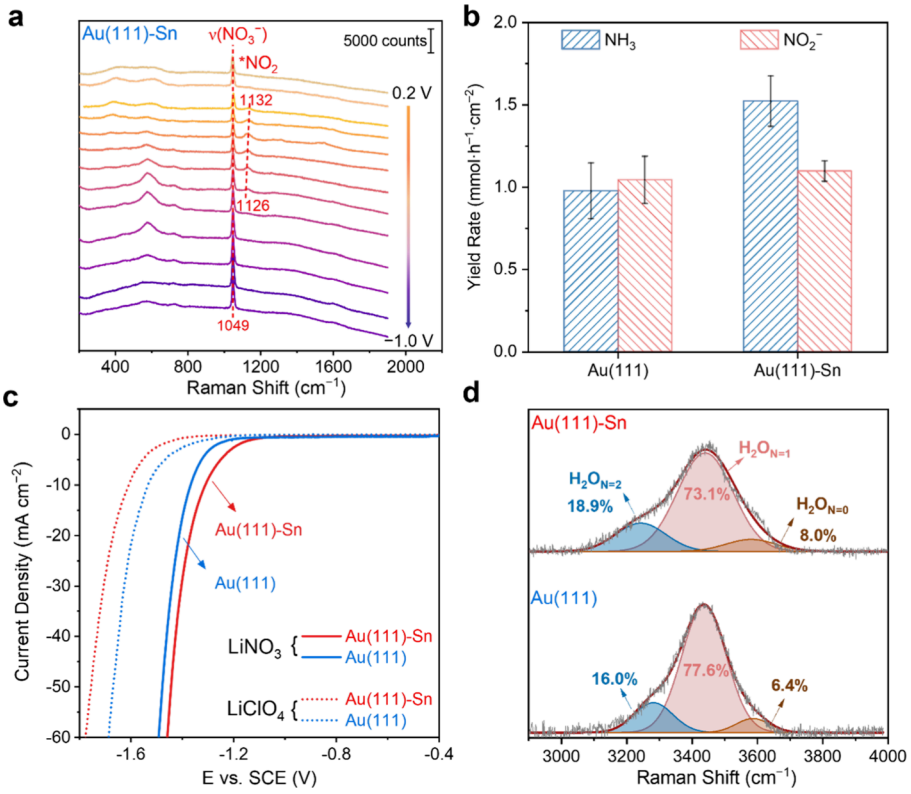


Figure 5. Sn-modification and interfacial H_2O structure (a) Potential-dependent intermediate evolution at Au(111)-Sn in 5.05 M $LiNO_3$ interface tracked by SHINERS. (b) Yield rates of NH_3 and NO_2^- on Au(111) and Au(111)-Sn. (c) LSV of Au(111) and Au(111)-Sn in 5.05 M $LiClO_4$ and $LiNO_3$. (d) Raman spectra of the O−H stretching mode of interfacial H_2O on Au(111) and Au(111)-Sn at −0.6 V. Gaussian fits of H_2O with 2, 1, and 0 donors are shown in blue, pink, and orange, respectively.

We employ a Sn-modified Au(111) single-crystal electrode (denoted as Au(111)-Sn) as a model system to test the hypothesis. The electrode was prepared via irreversible adsorption of Sn by immersing flame-annealed Au(111) in 0.1 M $HClO_4$ containing 10^{-4} M $SnSO_4$, followed by rinsing with Milli-Q water and electroreduction at negative potential.[37,38] We have conducted STM on a model Sn-modified Au(111) (Figure S21b). The results clearly show the presence of an amorphous Sn layer covering the Au surface, confirming the formation of a Sn−Au heterostructure. The successful modification was further confirmed by electrochemical and spectroscopic characterization. The CV of Au(111)-Sn in 0.05 M H_2SO_4 revealed a distinct oxidation peak at 0.1 V, attributed to the oxidation of Sn (Figure S22b), confirming the successful deposition of Sn. Additionally, the HER onset potential shifts negatively after Sn deposition, indicative of suppressed HER activity (Figure S22a). In situ SHINERS further verified the presence and chemical state of surface Sn species. Characteristic Sn−O vibrational modes (450 ∼ 550 cm^{-1}) emerge at 0.2 V in 1.00 M $LiNO_3$ (Figure S23), confirming the oxidation of Sn. These peaks were absent on pristine Au(111), while Au oxidation occurred only at potentials >1.0 V, establishing the formation of a stable Sn/Au(111) heterostructure within the reaction window.

XPS analysis further elucidates the electronic nature of this interface. The high-resolution Sn 3d spectrum indicates that Sn exists predominantly in an oxidized Sn(IV) state on the surface (Figure S25). Critically, a notable negative shift was observed in the Au 4f peak (from 84.83 to 83.84 eV) upon Sn modification, accompanied by corresponding O 1s features (Figures S24 and S26). This provides strong evidence for electron transfer from the Au substrate to the more electronegative Sn-oxide overlayer. This charge redistribution, which is dynamically tunable under reductive potentials, directly alters the electronic properties of the catalyst surface.

The impact of Sn on reaction kinetics was directly observed by in situ SHINERS. Compared to pristine Au(111), the characteristic $*NO_2$ Raman signal significantly decreased on the Au(111)-Sn surface at equivalent potentials (Figure 5a), indicating a reduced steady-state concentration of $*NO_2$. This suggests that Sn promotes faster $*NO_2$ consumption, likely by lowering the activation barrier for its hydrogenation to $*HNO_2$. DFT calculations support this view: Sn donates electrons to the Au surface, lowering the local d-band center and weakening $*NO_2$ adsorption. This electronic modulation facilitates $*NO_2$ hydrogenation and enhances NH_3 production.[39,40] Indeed, Au(111)-Sn exhibited a higher NH_3 yield with minimal NO_2^- byproduct (Figure 5b), underscoring its selectivity toward full reduction. Further mechanistic insights were obtained via LSV in 5.05 M $LiNO_3$ and $LiClO_4$. In $LiClO_4$, Sn modification delayed the HER onset, confirming its suppressive effect. In $LiNO_3$, both Au(111) and Au(111)-Sn showed positively shifted reduction potentials, but the Sn-modified surface exhibited a more favorable onset, indicating a synergistic enhancement of NO_3RR activity and HER suppression (Figure 5c).

Beyond electronic effects, Sn plays a crucial role in the engineering of the interfacial solvation environment, as revealed by in situ SHINERS analysis of the O−H stretching region. Deconvolution of the spectra (3000 to 3800 cm^{-1}) identified three types of interfacial water molecules: H_2O with 2 donors ($H_2O_{N=2}$) around 3200 to 3300 cm^{-1}, H_2O with 1

https://doi.org/10.1021/jacs.5c13376
J. Am. Chem. Soc. 2026, 148, 425−433

Downloaded from pubs.acs.org/jacsat/article-pdf/148/1/425/6337224/1/ja5c13376.pdf by UNIV TOWN OF SHENZHEN user on 08 September 2026

donor ($H_2O_{N=1}$) around 3300 to 3500 cm^{-1} and H_2O without any donor ($H_2O_{N=0}$) above 3500 cm^{-1}. Sn modification increased the proportion of both $H_2O_{N=2}$ and $H_2O_{N=1}$ (Figure 5d), indicating a more structured and proton-conductive water network. As a result, the proton-coupled electron transfer steps crucial for hydrogenation were accelerated.[41−44] This rearrangement enriches the interface with ion-interacted water molecules, forming a "proton superhighway" that facilitates rapid proton delivery to surface-bound intermediates, essential for deep reduction.[45,46] A more ordered water network is known to be more proton-conductive, accelerating the proton-coupled electron transfer (PCET) steps, such as the kinetically limiting $*NO_2 \rightarrow *NO_2H$ hydrogenation, by facilitating rapid proton delivery to the surface-bound intermediates. Beyond simply acting as a proton conduit, this highly organized hydrogen-bond network can also actively mediate interactions between coadsorbed species. As recently highlighted,[47,48] the interfacial hydrogen-bond network can mediate long-range interactions between adsorbates. At the significant coverages of $*NO_2$ observed in our study, lateral repulsive forces between adjacent $*NO_2$ species could be substantial. The more ordered water layer induced by Sn can act as an effective dielectric spacer, screening these repulsive interactions and stabilizing the adsorbate layer. This effect would further lower the overall energy barrier for the reaction, working in concert with the enhanced proton delivery.

In essence, the Sn-modification strategy transitions the system from one passively influenced by the double layer to one actively controlled by a coengineered, static-dynamic interface. The superior performance, including the more favorable NO_3RR onset and suppressed HER and enhanced NH_3 selectivity, is the direct outcome of this engineered synergy. This demonstrates a powerful design principle where the catalyst surface acts as an active scaffold to co-organize both the interfacial solvent and cations, enhancing the function of the entire interfacial system.

CONCLUSIONS

In summary, we have uncovered the pivotal role of the $*NO_2$ intermediate in governing the kinetics of electrocatalytic NO_3RR to NH_3 on Au single-crystal surfaces. Through a combination of in situ SHINERS and multiscale simulations, we identified $*NO_2$ as the central intermediate stabilized by electrolyte cations, and further revealed it as the kinetically critical step in the overall reaction pathway. Guided by this mechanistic insight, we introduced Sn heteroatom modification as a dual-function strategy to optimize both electronic interactions and interfacial solvation. Sn modulates the local electronic structure to weaken $*NO_2$ adsorption and simultaneously restructures the interfacial hydrogen-bond network to enhance proton-coupled electron transfer. These effects synergistically promote $*NO_2$ hydrogenation and suppress competing HER, enabling high NH_3 selectivity and reaction efficiency. This work demonstrates a comprehensive, molecular-level picture of the NO_3RR mechanism on Au surfaces. We have moved beyond a static picture of active sites to an integrated approach that considers the entire electrochemical interface, where atomic-scale electronic tuning is coupled with molecular-scale solvation control. Our central conclusion is that electrolyte cations act as pivotal kinetic modulators, and this insight directly enabled the rational design of a Sn-modified surface that enhances performance by creating a coengineered interfacial system. This study not only advances the understanding of nitrate reduction but also champions an integrated, mechanism-driven research paradigm that will be crucial for the future design of highly efficient catalysts for a wide range of complex electrochemical reactions.

ASSOCIATED CONTENT

Data Availability Statement

All DFT-optimized structures in the energy diagram and the full MD trajectories can be found at 10.5281/zenodo.17311444.

Supporting Information

The Supporting Information is available free of charge at https://pubs.acs.org/doi/10.1021/jacs.5c13376.

Detailed methods (synthesis, characterizations, electrochemical measurements, theoretical calculations) (PDF)

AUTHOR INFORMATION

Corresponding Authors

Yao-Hui Wang − *College of Materials, State Key Laboratory of Physical Chemistry of Solid Surfaces, iChEM, College of Chemistry and Chemical Engineering, College of Energy, School of Life Sciences, College of Physical Science and Technology, and Discipline of Intelligent Instrument and Equipment, Xiamen University, Xiamen 361005, China;* orcid.org/0000-0002-7311-9104; Email: yaohuiwang@xmu.edu.cn

Feng Pan − *School of Advanced Materials, Peking University, Shenzhen Graduate School, Shenzhen 518055, China;* orcid.org/0000-0002-8216-1339; Email: panfeng@pkusz.edu.cn

Jian-Feng Li − *College of Chemistry, Chemical Engineering and Environment, Minnan Normal University, Zhangzhou 363000, China; College of Materials, State Key Laboratory of Physical Chemistry of Solid Surfaces, iChEM, College of Chemistry and Chemical Engineering, College of Energy, School of Life Sciences, College of Physical Science and Technology, and Discipline of Intelligent Instrument and Equipment, Xiamen University, Xiamen 361005, China; Innovation Laboratory for Sciences and Technologies of Energy Materials of Fujian Province (IKKEM), Xiamen 361005, China; Liaoning Binhai Laboratory, Liaoning 115004, China;* orcid.org/0000-0003-1598-6856; Email: li@xmu.edu.cn

Authors

Ru-Yu Zhou − *College of Chemistry, Chemical Engineering and Environment, Minnan Normal University, Zhangzhou 363000, China; College of Materials, State Key Laboratory of Physical Chemistry of Solid Surfaces, iChEM, College of Chemistry and Chemical Engineering, College of Energy, School of Life Sciences, College of Physical Science and Technology, and Discipline of Intelligent Instrument and Equipment, Xiamen University, Xiamen 361005, China*

Shisheng Zheng − *College of Materials, State Key Laboratory of Physical Chemistry of Solid Surfaces, iChEM, College of Chemistry and Chemical Engineering, College of Energy, School of Life Sciences, College of Physical Science and Technology, and Discipline of Intelligent Instrument and Equipment, Xiamen University, Xiamen 361005, China; School of Advanced Materials, Peking University, Shenzhen Graduate School, Shenzhen 518055, China;* orcid.org/0009-0000-4529-7440

Downloaded from pubs.acs.org/jacsat/article-pdf/148/1/425/6337224/1/ja5c13376.pdf by UNIV TOWN OF SHENZHEN user on 08 September 2026

Rui Ma − *College of Materials, State Key Laboratory of Physical Chemistry of Solid Surfaces, iChEM, College of Chemistry and Chemical Engineering, College of Energy, School of Life Sciences, College of Physical Science and Technology, and Discipline of Intelligent Instrument and Equipment, Xiamen University, Xiamen 361005, China*

Mengting Zhao − *College of Materials, State Key Laboratory of Physical Chemistry of Solid Surfaces, iChEM, College of Chemistry and Chemical Engineering, College of Energy, School of Life Sciences, College of Physical Science and Technology, and Discipline of Intelligent Instrument and Equipment, Xiamen University, Xiamen 361005, China*

Chongyuan Zhai − *College of Materials, State Key Laboratory of Physical Chemistry of Solid Surfaces, iChEM, College of Chemistry and Chemical Engineering, College of Energy, School of Life Sciences, College of Physical Science and Technology, and Discipline of Intelligent Instrument and Equipment, Xiamen University, Xiamen 361005, China*

Jin-Chao Dong − *College of Materials, State Key Laboratory of Physical Chemistry of Solid Surfaces, iChEM, College of Chemistry and Chemical Engineering, College of Energy, School of Life Sciences, College of Physical Science and Technology, and Discipline of Intelligent Instrument and Equipment, Xiamen University, Xiamen 361005, China; Innovation Laboratory for Sciences and Technologies of Energy Materials of Fujian Province (IKKEM), Xiamen 361005, China;* orcid.org/0000-0001-7776-6360

Complete contact information is available at: https://pubs.acs.org/10.1021/jacs.5c13376

Author Contributions

[§]R.-Y.Z. and S.Z. contributed equally.

Notes

The authors declare no competing financial interest.

■ ACKNOWLEDGMENTS

This work was supported by grants from the National Natural Science Foundation of China (22322206, 22525042, 22472141, T2293692, and 22021001), the State Key Laboratory of Fine Chemicals, Dalian University of Technology (KF 2401), the Fundamental Research Funds for the Central Universities (20720240054), the Liaoning Binhai Laboratory (Grant No. 2024-05), and the Industry-University-Research Joint Innovation Project of Fujian Province, China (2025H6023).

■ REFERENCES

(1) Chen, J. G.; Crooks, R. M.; Seefeldt, L. C.; Bren, K. L.; Bullock, R. M.; Darensbourg, M. Y.; Holland, P. L.; Hoffman, B.; Janik, M. J.; Jones, A. K.; Kanatzidis, M. G.; King, P.; Lancaster, K. M.; Lymar, S. V.; Pfromm, P.; Schneider, W. F.; Schrock, R. R. Beyond Fossil Fuel-Driven Nitrogen Transformations. *Science* **2018**, *360* (6391), No. eaar6611.

(2) Liang, J.; Li, Z.; Zhang, L.; He, X.; Luo, Y.; Zheng, D.; Wang, Y.; Li, T.; Yan, H.; Ying, B.; Sun, S.; Liu, Q.; Hamdy, M. S.; Tang, B.; Sun, X. Advances in Ammonia Electrosynthesis from Ambient Nitrate/Nitrite Reduction. *Chem* **2023**, *9*, 1768−1827.

(3) Wang, T.; Zhao, Y.; Setzler, B. P.; Abbasi, R.; Gottesfeld, S.; Yan, Y. A High-Performance 75 W Direct Ammonia Fuel Cell Stack. *Cell Rep. Phys. Sci.* **2022**, *3* (4), No. 100829.

(4) Li, W.; Xu, M.; Chen, J.; Ye, T. Enabling Sustainable Ammonia Synthesis: From Nitrogen Activation Strategies to Emerging Materials. *Adv. Mater.* **2024**, *34* (40), No. 2408434.

(5) Qiang, S.; Wu, F.; Yu, J.; Liu, Y.; Ding, B. Complementary Design in Multicomponent Electrocatalysts for Electrochemical Nitrogen Reduction: Beyond the Leverage in Activity and Selectivity. *Angew. Chem. Int. Ed.* **2023**, *62* (15), No. e202217265.

(6) Li, L.; Tang, C.; Yao, D.; Zheng, Y.; Qiao, S.-Z. Electrochemical Nitrogen Reduction: Identification and Elimination of Contamination in Electrolyte. *ACS Energy Letters* **2019**, *4* (9), 2111−2116.

(7) Xu, H.; Ma, Y.; Chen, J.; Zhang, W. X.; Yang, J. Electrocatalytic Reduction of Nitrate-A Step towards A Sustainable Nitrogen Cycle. *Chem. Soc. Rev.* **2022**, *51* (7), 2710−2758.

(8) van Langevelde, P.; Katsounaros, I.; Koper, M. Electrocatalytic Nitrate Reduction for Sustainable Ammonia Production. *Joule* **2021**, *5* (2), 290−294.

(9) John, J.; MacFarlane, D. R.; Simonov, A. N. The Why and How of NO_x Electroreduction to Ammonia. *Nat. Catal.* **2023**, *6* (12), 1125−1130.

(10) Wan, Y.; Tang, Y.; Zuo, Y.; Sun, K.; Zhuang, Z.; Zheng, Y.; Yan, W.; Zhang, J.; Lv, R. Interfacial hydrogen bond modulation of dynamic catalysts for nitrate electroreduction to ammonia. *Energy Environ. Sci.* **2025**, *18*, 7460−7469.

(11) Zhang, K.; Zou, X.; Liu, Y.; Zhang, X.; An, L. Progress and Perspectives in the Electroreduction of Low-Concentration Nitrate for Wastewater Management. *iScience* **2025**, *28* (1), No. 111687.

(12) Fan, K.; Xie, W.; Li, J.; Sun, Y.; Xu, P.; Tang, Y.; Li, Z.; Shao, M. Active Hydrogen Boosts Electrochemical Nitrate Reduction to Ammonia. *Nat Commun* **2022**, *13*, 7958.

(13) Dong, J.; Song, X.; Chen, Y.; Gai, Z.; Yuan, Z.; Liu, D.; Tan, Z.; Liu, A.; Wang, X.; Song, S. Engineering Ce Promoter to Regulate H* Species to Boost Tandem Electrocatalytic Nitrate Reduction for Ammonia Synthesis. *Adv. Funct. Mater.* **2025**, *35* (25), No. 2422025.

(14) Ouyang, X.; Qiao, W.; Yang, Y.; Xi, B.; Yu, Y.; Wu, Y.; Fang, J.; Li, P.; Xiong, S. Intensifying Interfacial Reverse Hydrogen Spillover for Boosted Electrocatalytic Nitrate Reduction to Ammonia. *Angew. Chem. Int. Ed.* **2025**, *64* (13), No. e202422585.

(15) Qian, S.-J.; Cao, H.; Lv, X.-M.; Li, J.; Wang, Y.-G. Elucidating the Activity of Electrochemical Nitrate Reduction: High-Valent Anionic Intermediates as Kinetic Gatekeepers. *J. Am. Chem. Soc.* **2025**, *147* (24), 21032−21040.

(16) Kato, M.; Okui, M.; Taguchi, S.; Yagi, I. Electrocatalytic nitrate reduction on well-defined surfaces of tin-modified platinum, palladium and platinum-palladium single crystalline electrodes in acidic and neutral media. *J. Electroanal. Chem.* **2017**, *800*, 46−53.

(17) Gao, Q.; Yao, B.; Pillai, H. S.; Zang, W.; Han, X.; Liu, Y.; Yu, S.-W.; Yan, Z.; Min, B.; Zhang, S.; Zhou, H.; Ma, L.; Xin, H.; He, Q.; Zhu, H. Synthesis of Core/Shell Nanocrystals with Ordered Intermetallic Single-Atom Alloy Layers for Nitrate Electroreduction to Ammonia. *Nat. Synth.* **2023**, *2* (7), 624−634.

(18) Jia, S.; Zhang, L.; Liu, H.; Wang, R.; Jin, X.; Wu, L.; Song, X.; Tan, X.; Ma, X.; Feng, J.; Zhu, Q.; Kang, X.; Qian, Q.; Sun, X.; Han, B. Upgrading of Nitrate to Hydrazine through Cascading Electrocatalytic Ammonia Production with Controllable N-N Coupling. *Nat Commun* **2024**, *15* (1), 8567.

(19) Li, Y.; Lu, Z.; Zheng, L.; Yan, X.; Xie, J.; Yu, Z.; Zhang, S.; Jiang, F.; Chen, H. The Synergistic Catalysis Effect on Electrochemical Nitrate reduction at the Dual-Function Active Sites of the Heterostructure. *Energy Environ. Sci.* **2024**, *17* (13), 4582−4593.

(20) Wang, J.; Bui, H.; Wang, X.; Lv, Z.; Hu, H.; Kong, S.; Wang, Z.; Liu, L.; Chen, W.; Bi, H.; Yang, M.; Brinck, T.; Wang, J.; Huang, F. A Copper-Zinc Cyanamide Solid-Solution Catalyst with Tailored Surface Electrostatic Potentials Promotes Asymmetric N-Intermediate Adsorption in Nitrite Electroreduction. *J. Am. Chem. Soc.* **2025**, *147* (9), 8012−8023.

(21) Yao, Y.; Zhu, S.; Wang, H.; Li, H.; Shao, M. A Spectroscopic Study on the Nitrogen Electrochemical Reduction Reaction on Gold and Platinum Surfaces. *J. Am. Chem. Soc.* **2018**, *140* (4), 1496−1501.

(22) Li, J.-F.; Huang, Y.-F.; Ding, Y.; Yang, Z.-L.; Li, S.-B.; Zhou, X.-S.; Fan, F.; Zhang, W.; Zhou, Z.-Y.; Wu, D.-Y.; Ren, B.; Wang, Z.-L.; Tian, Z.-Q. Shell-Isolated Nanoparticle-Enhanced Raman Spectroscopy. *Nature* **2010**, *464* (7287), 392−395.

Downloaded from pubs.acs.org/jacsat/article-pdf/148/1425/6337224l/ja5c13376.pdf by UNIV TOWN OF SHENZHEN user on 08 September 2026

(23) Li, J.-F.; Tian, X.-D.; Li, S.-B.; Anema, J. R.; Yang, Z.-L.; Ding, Y.; Wu, Y.-F.; Zeng, Y.-M.; Chen, Q.-Z.; Ren, B.; Wang, Z.-L.; Tian, Z.-Q. Surface Analysis using Shell-Isolated Nanoparticle-Enhanced Raman Spectroscopy. *Nat. Protoc.* **2013**, *8* (1), 52−65.
(24) Fang, J. Y.; Zheng, Q. Z.; Lou, Y. Y.; Zhao, K. M.; Hu, S. N.; Li, G.; Akdim, O.; Huang, X. Y.; Sun, S. G. Ampere-level Current Density Ammonia Electrochemical Synthesis using CuCo Nanosheets Simulating Nitrite Reductase Bifunctional Nature. *Nat Commun* **2022**, *13* (1), 7899.
(25) Wang, Y.-H.; Li, S.; Zhou, R.-Y.; Zheng, S.; Zhang, Y.-J.; Dong, J.-C.; Yang, Z.-L.; Pan, F.; Tian, Z.-Q.; Li, J.-F. In situ Electrochemical Raman Spectroscopy and Ab Initio Molecular Dynamics Study of Interfacial Water on a Single-Crystal Surface. *Nat. Protoc.* **2023**, *18* (3), 883−901.
(26) Fang, Y.; Ding, S.-Y.; Zhang, M.; Steinmann, S. N.; Hu, R.; Mao, B.-W.; Feliu, J. M.; Tian, Z.-Q. Revisiting the Atomistic Structures at the Interface of Au(111) Electrode-Sulfuric Acid Solution. *J. Am. Chem. Soc.* **2020**, *142* (20), 9439−9446.
(27) Yang, Y.; Sun, Y.; Wang, Y.; Zhang, X.; Zhang, W.; Huang, Z.-F.; Yin, L.; Han, A.; Liu, G. Self-Triggering a Locally Alkaline Microenvironment of Co_4Fe_6 for Highly Efficient Neutral Ammonia Electrosynthesis. *J. Am. Chem. Soc.* **2025**, *147* (10), 8893−8905.
(28) Dong, J.-C.; Zhang, X.-G.; Briega-Martos, V.; Jin, X.; Yang, J.; Chen, S.; Yang, Z.-L.; Wu, D.-Y.; Feliu, J. M.; Williams, C. T.; Tian, Z.-Q.; Li, J.-F. In Situ Raman Spectroscopic Evidence for Oxygen Reduction Reaction Intermediates at Platinum Single-Crystal Surfaces. *Nat. Energy* **2019**, *4* (1), 60−67.
(29) Dong, J.-C.; Su, M.; Briega-Martos, V.; Li, L.; Le, J.-B.; Radjenovic, P.; Zhou, X.-S.; Feliu, J. M.; Tian, Z.-Q.; Li, J.-F. Direct In Situ Raman Spectroscopic Evidence of Oxygen Reduction Reaction Intermediates at High-Index Pt(hkl) Surfaces. *J. Am. Chem. Soc.* **2020**, *142* (2), 715−719.
(30) Zheng, J.; Tan, G.; Shan, P.; Liu, T.; Hu, J.; Feng, Y.; Yang, L.; Zhang, M.; Chen, Z.; Lin, Y.; Lu, J.; Neuefeind, J. C.; Ren, Y.; Amine, K.; Wang, L.-W.; Xu, K.; Pan, F. Understanding Thermodynamic and Kinetic Contributions in Expanding the Stability Window of Aqueous Electrolytes. *Chem.* **2018**, *4* (12), 2872−2882.
(31) Yang, Z.-L.; Zhu, Y.-Z.; Zhang, Y.-J.; Li, J.-F. Surface-Enhanced Raman Spectroscopy Study in the Reaction Process of Fuel Cells and Lithium Battery. *Chin. J. Light Scatt.* **2023**, *35* (2), 97−107.
(32) Zhang, L.; Zhou, H.; Yang, X.; Zhang, S.; Zhang, H.; Yang, X.; Su, X.; Zhang, J.; Lin, Z. Boosting Electroreduction Kinetics of Nitrogen to Ammonia via Atomically Dispersed Sn Protuberance. *Angew. Chem. Int. Ed.* **2023**, *62* (13), No. e202217473.
(33) Liu, H.; Cao, X.; Ding, L.; Wang, H. Sn-Doped Black Phosphorene for Enhancing the Selectivity of Nitrogen Electroreduction to Ammonia. *Adv. Funct. Mater.* **2022**, *32* (19), No. 2111161.
(34) Zhang, H.; Xu, D.; Yang, F.; Xie, J.; Liu, Q.; Liu, D.-J.; Zhang, M.; Lu, X.; Meng, Y. S. A High-Capacity Sn Metal Anode for Aqueous Acidic Batteries. *Joule* **2023**, *7* (5), 971−985.
(35) Kuriganova, A.; Smirnova, N. New Insights into Controlling the Functional Properties of Tin Oxides-Based Materials. *J. Electrochem.* **2025**, *31* (1), No. 2408261.
(36) Rodes, A.; Feliu, J. M.; Aldaz, A.; Clavilier, J. Irreversible Tin Adsorption on Polyoriented Gold electrodes. *J. Electroanal. Chem. Interfacial Electrochem.* **1988**, *256*, 455−462.
(37) Rodes, A.; Herrero, E.; Feliu, J. M.; Aldaz, A. Structure Sensitivity of Irreversibly Adsorbed Tin on Gold Single-Crystal Electrodes in Acid Media. *J. Chem. Soc., Faraday Trans.* **1996**, *92* (20), 3769−3776.
(38) Kato, M.; Unuma, Y.; Okui, M.; Qu, Y.; Zheng, J.; Taguchi, S.; Kiguchi, F.; Torihata, M.; Gao, Y.; Hoshi, N.; Yagi, I. Electrocatalytic Activity and Volatile Product Selectivity for Nitrate Reduction at Tin-Modified Pt(100), Pd(100) and Pd-Pt(100) Single Crystal Electrodes in Acidic Media. *Electrochim. Acta* **2021**, *398*, No. 139281.
(39) Sadhukhan, P.; Barman, S.; Roy, T.; Singh, V. K.; Sarkar, S.; Chakrabarti, A.; Barman, S. R. Electronic Structure of Au-Sn Compounds Grown on Au(111). *Phys. Rev. B* **2019**, *100* (23), No. 235404.
(40) Zhao, Y.; Wang, X.; Yang, S.; Kuttner, E.; Taylor, A. A.; Salemmilani, R.; Liu, X.; Moskovits, M.; Wu, B.; Dehestani, A.; Li, J.-F.; Chisholm, M. F.; Tian, Z.-Q.; Fan, F.-R.; Jiang, J.; Stucky, G. D. Protecting the Nanoscale Properties of Ag Nanowires with a Solution-Grown SnO_2 Monolayer as Corrosion Inhibitor. *J. Am. Chem. Soc.* **2019**, *141* (35), 13977−13986.
(41) Waegele, M. M. Water Molecules Directed to Speed Up Dissociation. *Nature* **2021**, *600*, 43−44.
(42) Wan, Y.; Pei, M.; Tang, Y.; Liu, Y.; Yan, W.; Zhang, J.; Lv, R. Interfacial Water Regulation for Nitrate Electroreduction to Ammonia at Ultralow Overpotentials. *Adv. Mater.* **2025**, *37* (8), No. 2417696.
(43) Wang, Y.-H.; Zheng, S.; Yang, W.-M.; Zhou, R.-Y.; He, Q. F.; Radjenovic, P.; Dong, J.-C.; Li, S.; Zheng, J.; Yang, Z.-L.; Attard, G.; Pan, F.; Tian, Z.-Q.; Li, J.-F. In Situ Raman Spectroscopy Reveals the Structure and Dissociation of Interfacial Water. *Nature* **2021**, *600* (7887), 81−85.
(44) Guha, A.; Sahoo, M.; Alam, K.; Rao, D. K.; Sen, P.; Narayanan, T. N. Role of Water Structure in Alkaline Water Electrolysis. *iScience* **2022**, *25* (8), No. 104835.
(45) Hu, Q.; Yang, K.; Peng, O.; Li, M.; Ma, L.; Huang, S.; Du, Y.; Xu, Z.-X.; Wang, Q.; Chen, Z.; Yang, M.; Loh, K. P. Ammonia Electrosynthesis from Nitrate Using A Ruthenium-Copper Cocatalyst System: A Full Concentration Range Study. *J. Am. Chem. Soc.* **2024**, *146* (1), 668−676.
(46) Zheng, S.; Yang, X.; Shi, Z.-Z.; Ding, H.; Pan, F.; Li, J.-F. The Loss of Interfacial Water-Adsorbate Hydrogen Bond Connectivity Position Surface-Active Hydrogen as A Crucial Intermediate to Enhance Nitrate Reduction Reaction. *J. Am. Chem. Soc.* **2024**, *146* (39), 26965−26974.
(47) Mom, R. V. Repulsion attractive for electrocatalysis. *Nat. Catal.* **2024**, *7*, 757−758.
(48) van der Heijden, O.; Eggebeen, J. J. J.; Trzesniowski, H.; Deka, N.; Golnak, R.; Xiao, J.; van Rijn, M.; Mom, R. V.; Koper, M. T. M. Li^+ Cations Activate NiFeOOH for Oxygen Evolution in Sodium and Potassium Hydroxide. *Angew. Chem. Int. Ed.* **2024**, *63* (18), No. e202318692.

Downloaded from pubs.acs.org/jacsat/article-pdf/148/1/425/6337224/1/ja5c13376.pdf by UNIV TOWN OF SHENZHEN user on 08 September 2026

https://doi.org/10.1021/jacs.5c13376
J. Am. Chem. Soc. 2026, 148, 425−433